Physics based Modeling for Time-Frequency Damage Classification

Debejyo Chakraborty*[a], Sunilkumar Soni[b], Jun Wei[b], Narayan Kovvali[a], Antonia Papandreou-Suppappola[a], Douglas Cochran[a], and Aditi Chattopadhyay[b]

[a]Department of Electrical Engineering, Arizona State University, Tempe, AZ
[b]Department of Mechanical and Aerospace Engineering, Arizona State University, Tempe, AZ

ABSTRACT

We have recently proposed a method for classifying waveforms from healthy and damaged structures in a structural health monitoring framework. This method is based on the use of hidden Markov models with preselected feature vectors obtained from the time-frequency based matching pursuit decomposition. In order to investigate the performance of the classifier for different signal-to-noise ratios (SNR), we simulate the response of a lug joint sample with different crack lengths using finite element modeling (FEM). Unlike experimental noisy data, the modeled data is noise free. As a result, different levels of noise can be added to the modeled data in order to obtain the true performance of the classifier under additive white Gaussian noise. We use the finite element package ABAQUS to simulate a lug joint sample with different crack lengths and piezoelectric sensor signals. A mesoscale internal state variable damage model defines the progressive damage and is incorporated in the macroscale model. We furthermore use a hybrid method (boundary element-finite element method) to model wave reflection as well as mode conversion of the Lamb waves from the free edges and scattering of the waves from the internal defects. The hybrid method simplifies the modeling problem and provides better performance in the analysis of high stress gradient problems.

Keywords: structural health monitoring, physics based modeling, damage detection, time-frequency analysis, matching pursuit decomposition, hidden Markov models

1. INTRODUCTION

An important problem encountered in structural health monitoring (SHM)[1–3] is the efficient detection and classification of damage in complex metallic structures. Some recent techniques in use for SHM include Lamb wave methods, wavelet transforms, impedance based approaches, statistical pattern recognition using outliers, artificial neural networks, and time-frequency (TF) analysis.[4,5] The key challenge in the design of a reliable damage detection system is the ability to account for the variability inherent in structural data. This variability might arise due to material properties, geometry variation, sensor characteristics, debonding issues, measurement noise, or other environmental factors such as temperature.

A stochastic time-frequency based damage classification approach was proposed[6] by the authors. Therein, time-frequency damage features are extracted from the structural data using the matching pursuit decomposition (MPD) algorithm.[7] The features are then processed using a stochastic technique known as hidden Markov modeling (HMM). The HMM models the data with a (hidden) Markov random process and inference is performed efficiently in a Bayesian framework.

In this paper, we extend that work by studying the robustness of the HMM based damage classifier to variability in sensor data due to the presence of noise. Data obtained numerically from the physics-based models[8–12] via finite element (FE) simulations[13] is used as a noise-free baseline to study the effect of noise on the classifier's performance. To do this, the algorithm is trained on the noise-free data and tested on data with controlled amounts of additive white Gaussian noise. We present results from an application to the classification of (simulated) crack-length in a lug-joint, demonstrating the utility of the proposed approach and the robustness of the classifier to noise.

*debejyo@asu.edu; phone 1 619 838 7334

Modeling, Signal Processing, and Control for Smart Structures 2008, edited by Douglas K. Lindner
Proc. of SPIE Vol. 6926, 69260M, (2008) · 0277-786X/08/$18 · doi: 10.1117/12.776628

The remainder of the paper is organized as follows. A background of the theoretical framework of MPD and HMM is provided followed by HMM based classification scheme in Section 2. In Section 3 we refer to and introduce the three dimensional FEM modeling. The modeling parameters and approach has been described in brief followed by the use of MPD as a feature extraction scheme and matching pursuit based time-frequency representation (MPD-TFR) as a cross-term free time-frequency representation. The later part of this section discusses the modeling of damage classes using HMM and the classification approach as applied to this problem. In results we have presented the performance the classifier as a function of noise and provided confusion matrices and receiver operating characteristic (ROC) curve as a measure of the performance. We conclude in Section 4 and summarize the future directions for this work and the immediate progress that we are considering.

2. HIDDEN MARKOV MODEL BASED DAMAGE CLASSIFIER

In this section we briefly review the analytical framework used in the proposed damage classification algorithm. For more details on these topics, the reader is referred to the literature.[7, 14, 15]

2.1 Matching Pursuit Decomposition

The matching pursuit decomposition (MPD) is an iterative method of representing a signal as a linear combination of basis functions or atoms chosen from a complete dictionary.[7] Any signal $x(t)$ can be represented as

$$x(t) = \sum_{i=0}^{\infty} \alpha_i \, g_i(t). \tag{1}$$

The atom $g_i(t)$ is chosen such that it maximizes the magnitude of the inner-product

$$\left\langle \left(x(t) - \sum_{r=0}^{i-1} \alpha_r \, g_r(t) \right), g_i(t) \right\rangle.$$

In practical applications, this expansion may be truncated to a finite N as

$$\hat{x}(t) = \sum_{i=0}^{N-1} \alpha_i \, g_i(t), \tag{2}$$

where $\hat{x}(t)$ is the approximate reconstruction of $x(t)$ and is referred to as the reconstructed signal. The truncation limit N in (2) is usually chosen such that the energy of the residue after N iterations is smaller than some predefined value. The residue $x(t) - \hat{x}(t)$ generally has a very small percentage of the overall signal energy and is ignored in subsequent analysis. The MPD is designed to provide the most compact representation of the given signal in terms of atoms. In addition, it effectively filters out unwanted signal components such as noise because the noise subspace is typically orthogonal to that spanned by the dictionary elements. In our application, we conside a dictionary of the form

$$g^{(d)}(t) = \left(\frac{8\kappa_l}{\pi} \right)^{\frac{1}{4}} e^{-\kappa_l \, (t-\tau_n)^2} \cos\left(2\pi\nu_m (t-\tau_n)\right), \tag{3}$$

which is a real Gaussian signal. Each dictionary with element $d = \{\tau_n, \nu_m, \kappa_l\}$ is a set of all time shifted (by τ_n, $n = 1, \ldots, N_d$), frequency shifted (by ν_m, $m = 1, \ldots, M_d$), and time scaled (by κ_l, $l = 1, \ldots, L_d$) atoms that are normalized to have unit energy. The overall dictionary of all transformed atoms is denoted by $\mathcal{D}$. In the remaining of the document we would use d as a feature vector and a set of d_i, $i = 0, \ldots, N-1$ would represent a signal entirely.

The MPD result is also used to define a time-frequency representation (MPD-TFR) which is defined as[7]

$$\mathscr{E}_x(t,f) = \sum_{i=0}^{N-1} |\alpha_i|^2 \, \mathbf{WD}_{g_i}(t,f), \tag{4}$$

where $\mathbf{WD}_{g_i}(t,f)$ is the Wigner distribution[16] of the atom chosen at the ith MPD iteration. This representation is a cross-term free approximation of the true Wigner distribution of the signal.

2.2 Hidden Markov Models

A hidden Markov model (HMM)[14,15] is a probabilistic model used for modeling sequential data. The HMM defines a probability distribution over an observation sequence $\mathbf{y} = \{y_n\}$, $n = 1, \ldots, T$ by invoking a sequence of hidden discrete variables $\mathbf{x} = \{x_n\}$, $n = 1, \ldots, T$ known as 'states'. The observations y_n are considered independent of all other variables given x_n and the model imposes Markov dynamics on the sequence x_n.

For an S state HMM with state variables x_s assuming values from the alphabet $\{1, \ldots, S\}$, the model can be parameterized by $\boldsymbol{\theta} = \{\pi, A, B\}$ where, π is an $S \times 1$ initial state distribution vector where the ith element is the probability $p(x_1 = i)$, A is an $S \times S$ state-transition matrix where the (i, j)th element is $p(x_{n+1} = j | x_n = i)$ and B is a state-dependent observation density matrix with its jth element denoted as $b_j(y_n) = p(y_n | x_n = j)$. For a *discrete* HMM, the observations y_n are discrete (restricted to V symbols) and B reduces to a $S \times V$ matrix whose (j, k)th element is $b_{jk} = p(y_n = v_k | x_n = j)$.

Given a 'training' observation sequence $\mathbf{y}$,* one can define an S state HMM λ_S that maximizes the probability of the observing the training sequence $y(n)$. This is done by computing the maximum-likelihood estimate of $\boldsymbol{\theta}$:

$$\boldsymbol{\theta}_{\mathrm{ML}} = \arg\max_{\boldsymbol{\theta}} \log p(\mathbf{y} | \boldsymbol{\theta}, \lambda_S) \tag{5}$$

using the Baum-Welch algorithm.[14,15] This is a special case of the expectation-maximization (EM) algorithm[17] which iteratively maximizes the likelihood of the training data. The details of the HMM reestimation procedure and relevant formulae can be found in[15] the paper by Rabiner.

The predictive likelihood of a 'test' observation sequence $\mathbf{y}'$ can then be estimated as

$$\begin{aligned} p(\mathbf{y}' | \boldsymbol{\theta}_{\mathrm{ML}}, \lambda_S) &= \sum_{\mathbf{x}} p(\mathbf{x}, \mathbf{y}' | \boldsymbol{\theta}_{\mathrm{ML}}, \lambda_S) \\ &= \sum_{\mathbf{x}} \pi_{x_1} \prod_{n=1}^{N-1} a_{x_n x_{n+1}} \prod_{n=1}^{N} b_{x_n}(y_n). \end{aligned} \tag{6}$$

Note that calculating the predictive likelihood from (6) directly is expensive (requires $2T \times S^T$ operations) but it can be efficiently computed using the forward-backward procedure[15] that has a complexity of $S^2 N$. A scaling procedure[15] ensures that the implementation is numerically stable in finite-precision arithmetic.

2.3 HMM Based Classification Algorithm

The critical first step of a successful classification system is the extraction of effective discriminatory features. In this work, MPD is applied to each signal. A set of MPD feature vectors $\{d_i\}$ obtained as described in Section 2.1 is used as features. A signal can be represented by vector $O = [o_0, o_1, \ldots, o_{N-1}]^T$ of observation sequence where $o_i = d_i$, $i = 0, \ldots, N-1$. It may be noted that the sequence length is the same as the number MPD iterations as the MPD features are directly used as the observation sequence for the HMM. A subset of such observation sequences belonging to different damage classes is used for training HMM models for each class. The remaining observation sequences may be used for model validation and testing. The classifier assigns a given test observation sequence $\mathbf{y}'$ to damage class k, given by

$$k = \underset{j}{\mathrm{argmax}} \left\{ p(\mathbf{y}' | \boldsymbol{\theta}_{\mathrm{ML}}^{(j)}, \lambda_S) \right\}, \tag{7}$$

where $\boldsymbol{\theta}_{\mathrm{ML}}^{(j)}$ denotes the parameters of the jth HMM (trained on data from damage class j).

3. APPLICATION TO THE DETECTION OF FATIGUE INDUCED DAMAGE

In this section, we study the performance of the HMM based classifier in the presence of noise. To start with, we needed a noise-free signal. The FEM based modeling that is discussed in 3.1 is used to obtain the clean signal. Different levels of noise was added to this signal and performance of the HMM classifier was tested in each case. In addition, it is notable in this section that MPD can be used as a filter to remove noise from the signal.

*For simplicity here we consider just a single observation sequence; the treatment is easily extended to a data set comprising of multiple independent and identically distributed observation sequences.

3.1 Physics Based Three-Dimensional Finite Element Modeling of Lug Joint Sample

The lug sample modeled is shown in Figure 1(a). The considered sample was made from 0.25 in. thick Al 2024-T3 alloy plate with a polished surface finish. The dimensions of the sample are shown in Figure 1(b). The

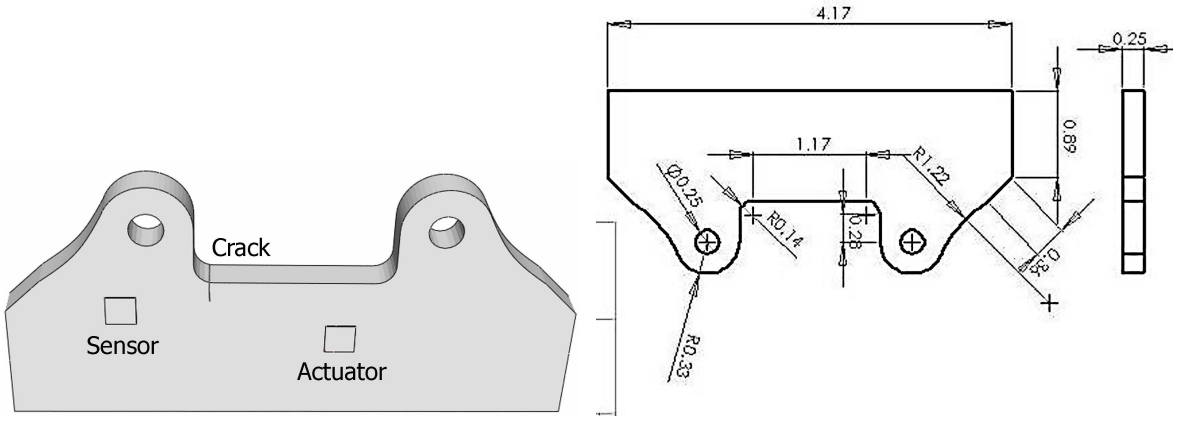

(a) Sensor placement and sight of crack. (b) Dimensionality.

Figure 1. Modeled lug joint sample showing sensor location, crack and dimensions.

model essentially had three parts: the lug, PZT and an adhesive layer as shown in Figure 2(b). The lug and the adhesive layer each were modeled as isotropic, homogeneous material. The properties for alumina 2024/T351 were assigned to the lug. Continuum three-dimensional brick elements (C3D8R) were used to model both. In the lug model, the size of the mesh was different for samples with different levels of crack (notch) lengths. In this model, a crack length of 6 mm was considered. The PZT was modeled as an orthotropic material with the properties defined in the local orientation system and continuum three-dimensional piezoelectric elements were used. A Tie constraint was used to define the interaction between the lug and the adhesive layer and also between the adhesive layer and the PZTs.

With these model specifications, a three-dimensional finite element modeling (FEM) was carried out for the lug sample discussed above using the commercial finite element software ABAQUS/Standard (see Figure 2(a)).

All the degrees of freedom were suppressed at one of the nodes of the lug as indicated at the bottom right corner in Figure 2(a). A peak to peak voltage of 100 V was applied to the upper surface of the PZT while the bottom surface was maintained at zero volts. A tone burst signal with central frequency 130 KHz was used as the actuation signal.

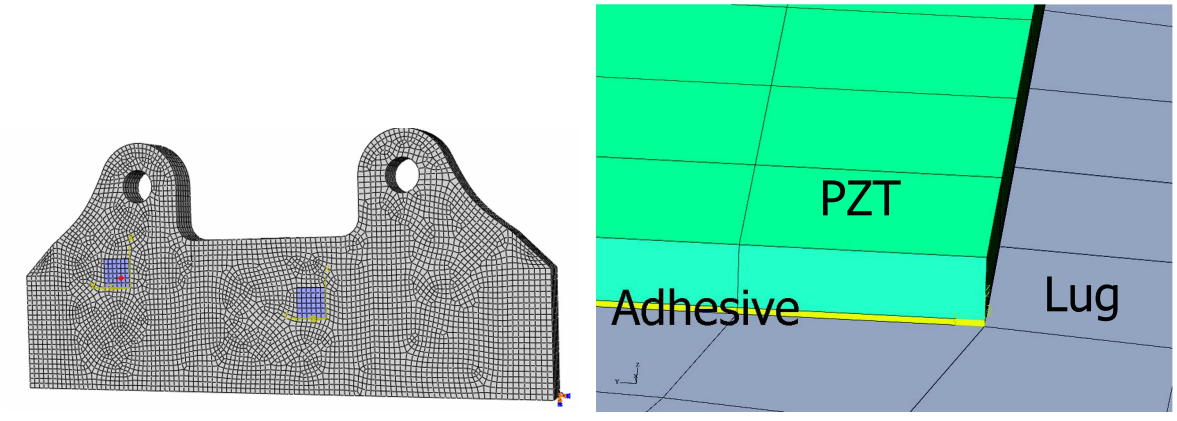

(a) Lug sample showing three-dimensional elements. (b) Lug, adhesive and PZT layers.

Figure 2. Three-dimensional FEM with boundary condition and layers.

In our specific problem, to solve the wave propagation in lug joints, the elastodynamic wave equation is solved using FEM. The specific geometry was defined in the ABAQUS software. The basic elastodynamic equation in a homogeneous anisotropic solid can be written as[18]

$$C_{ijkl}(x_n)\frac{\partial^2}{\partial x_j x_l}u_k(x_n,t) + F_i(x_n,t) = \rho(x_n)\frac{\partial^2 u_i(x_n,t)}{\partial^2 t}, \tag{8}$$

where $C_{ijkl}(x_n)$ are the material constants, u_i are the displacement components F_i denotes the body force per unit volume and i, j, k, l and n take values 1, 2 and 3. In the subsequent formulation, all subscripts correspond to the usual index notation in three-dimensional space, and δ_{ij} is the Kronecker delta symbol. However, considering the aluminum specimen as the isotopic material used for our experiment and modeling the elastodynamic equation reduced to

$$(\lambda + 2\mu)u_{j,ij} - \mu\epsilon_{ijk}\epsilon_{kmn}u_{n,mj} + P_i f(t)\delta(x_p) = \rho\ \ddot{u}_i\ . \tag{9}$$

Here λ and μ are two Lame' constants of aluminum material. P_i is the magnitude of the external force provided on the body and $f(t)$ is the time dependent unit wave packet acting on the body. Hence, the particle in motion is subjected to time dependent excitation. Please note that the above expressions are valid at a point in the body. To solve a global problem, external force is provided by an actuator with the burst wave as specified earlier. Hence, each point in the body is subjected to external time dependent force and the problem is solved by modeling the problem in ABAQUS. Fixed time steps were considered to solve the problem and isoparametric elements were used to model the complete body. The traction free boundary condition was provided at the lug joint boundary.

In this example, two damage cases were modeled. One was unfatigued (with no defects) and the other was fatigued (with a 6 mm crack).

3.2 Data Synthesis and Feature Extraction using Matching Pursuit Decomposition

The data obtained from the modeling result discussed in 3.1, is deterministic. We had synthetically added white Gaussian noise to introduce randomness in the otherwise deterministic process. Signal-to-noise ratio (SNR) is the measure of added noise used and is defined as

$$\text{SNR} = 10\log_{10}\left[\frac{\sum_{n=0}^{L-1} x^2(n)}{L\sigma^2}\right]\ \text{dB}, \tag{10}$$

where L is the length of the signal ($L = 512$ in this application) and σ^2 is the variance of the noise. We chose SNRs of -3 through 5 dB, 10 dB, 15 dB and 20 dB. The very low noise 20 dB signal was considered representative (noise free) class and the HMM was trained on it. We had synthesized 450 signal realizations at each SNR for each damage case. It may be noted that all the signals (with added noise) were normalized to unit energy. These time domain signals (Figures 3(a) and 3(b)) were not separable enough to identify the class of damage. In fact, with lower SNR, the difference between the time series representing two classes of damage reduces even further as shown in Figures 4(a) and 4(b). The analysis of signals was extended to a joint time-frequency plane to pursue the instantaneous frequency content of the signals. A common time-frequency representation called the spectrogram was used for this purpose. Figures 3(c) and 3(d) compare the spectrograms of the healthy and the damaged signals at 20 dB. A similar comparison is shown at 0 dB in figures 4(c) and 4(d). The presence of in-band noise can be observed.

The MPD was performed on these signals as described in Section 2.1. The dictionary $\mathcal{D}$ was composed of 33 million time and frequency shifted Gaussian atoms as in (3) of various scales spanning 25 KHz to 225 KHz over all times. Example spectrograms as in Figures 3(c) and 3(d) show that most of the information is in this band of frequencies. Figures 3(e) and 3(f) show the time series generated by the MPD reconstruction as shown in Equation (2). The signals reconstructed after the MPD had reduced noise (both in-band and out-of-band) and retained the predominant characteristic information pertaining to each class of damage as shown in Figures 3(g)

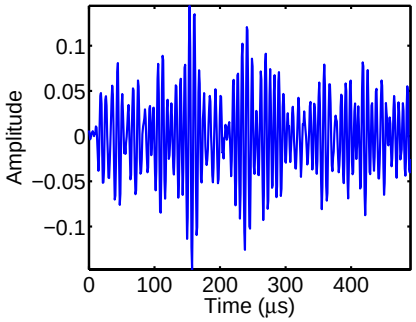

(a) Unfatigued

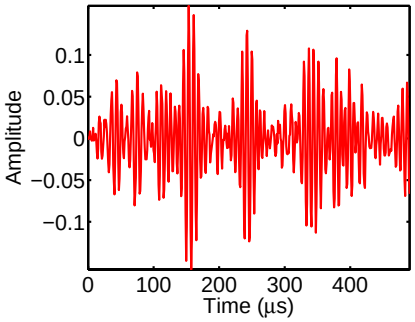

(b) Fatigued

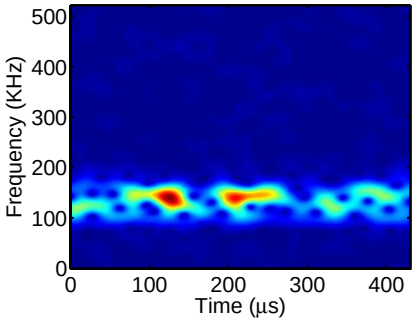

(c) Spectrogram of unfatigued case

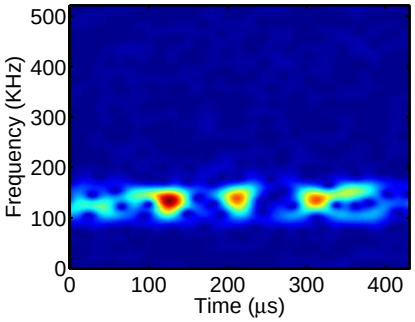

(d) Spectrogram of fatigued case

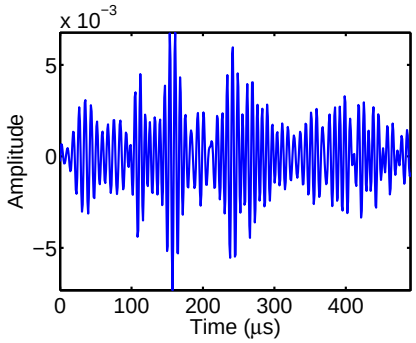

(e) MPD reconstruction for unfatigued case

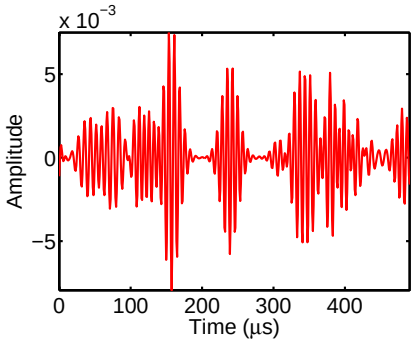

(f) MPD reconstruction for fatigued case

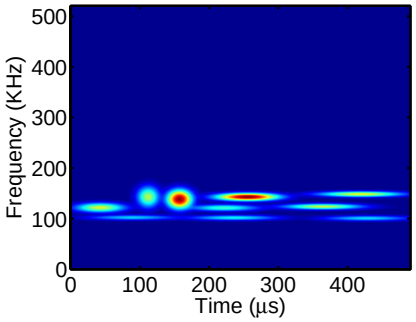

(g) MPD-TFR of unfatigued case

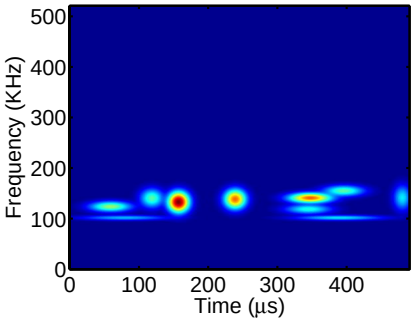

(h) MPD-TFR of fatigued case

Figure 3. Time and TFR plots of example waveforms from unfatigued and fatigued data at 20 dB SNR.

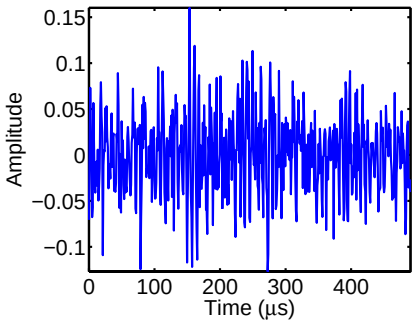

(a) Unfatigued

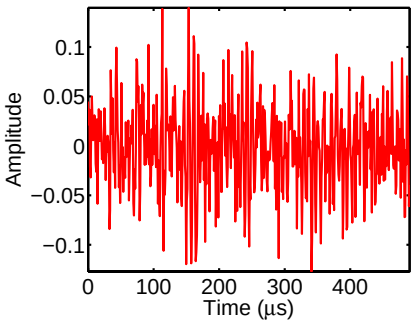

(b) Fatigued

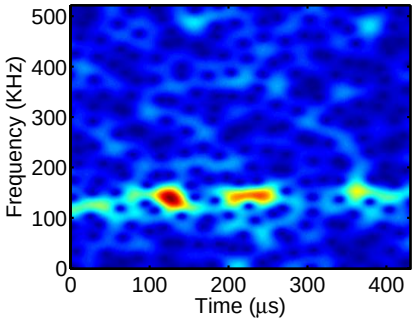

(c) Spectrogram of unfatigued case

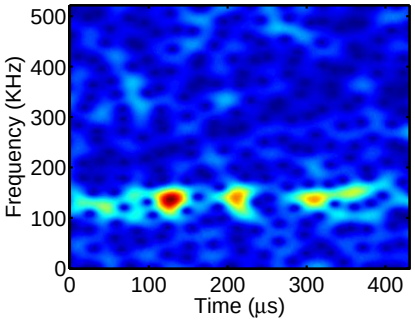

(d) Spectrogram of fatigued case

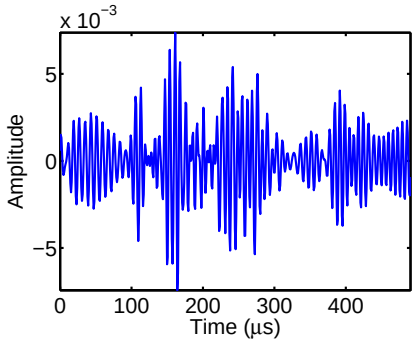

(e) MPD reconstruction for unfatigued case

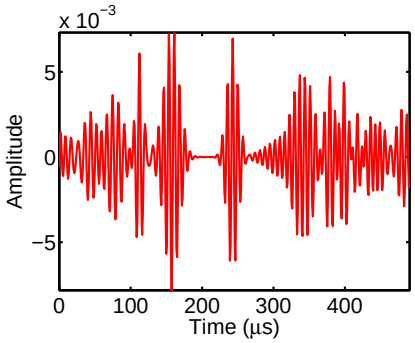

(f) MPD reconstruction for fatigued case

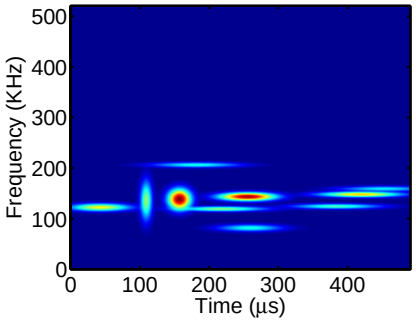

(g) MPD-TFR of unfatigued case

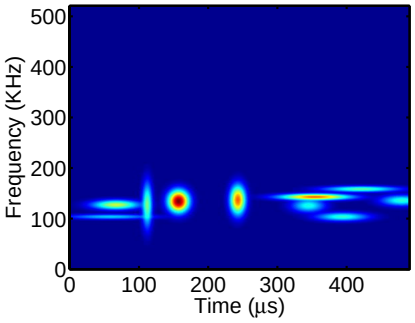

(h) MPD-TFR of fatigued case

Figure 4. Time and TFR plots of example waveforms from unfatigued and fatigued data at 0 dB SNR.

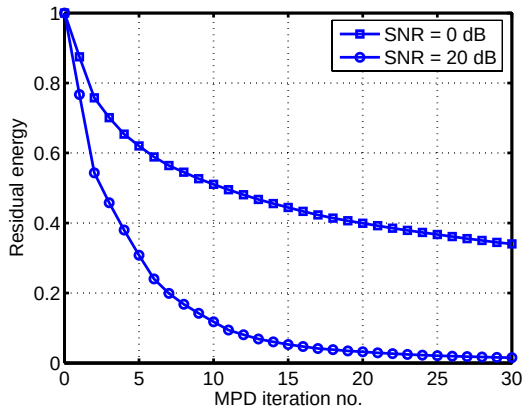

(a) MPD error for unfatigued.

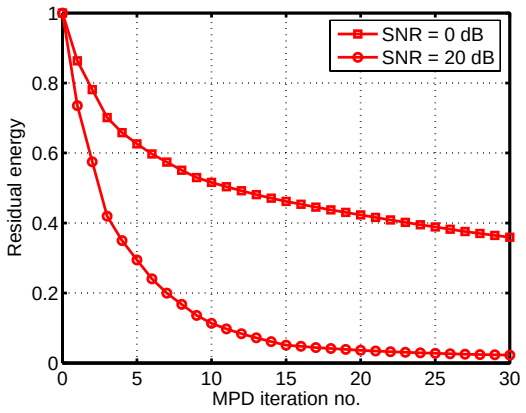

(b) MPD error for fatigued.

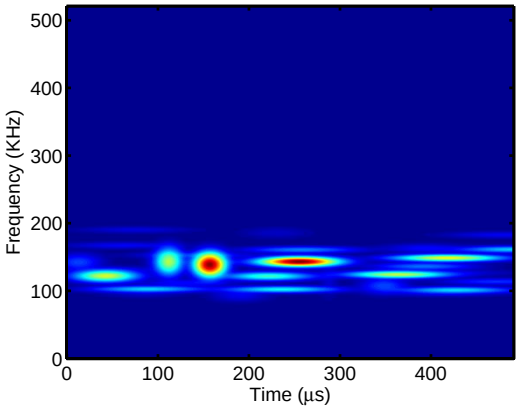

(c) MPD-TFR of unfatigued case with SNR = 20 dB.

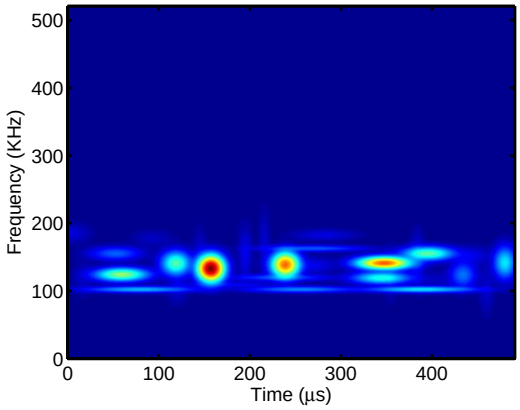

(d) MPD-TFR of fatigued case with SNR = 20 dB.

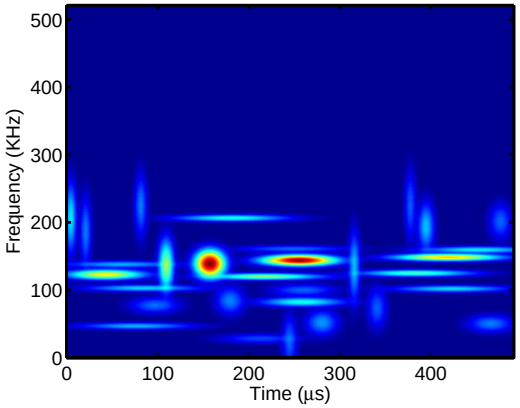

(e) MPD-TFR of fatigued case with SNR = 0 dB.

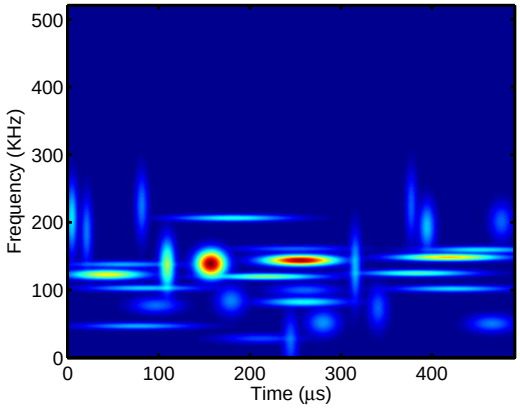

(f) MPD-TFR of fatigued case with SNR = 0 dB.

Figure 5. Effect of noise on MPD residual error and TFR reconstruction (for 30 iterations).

and 3(h). These MPD-TFRs are constructed according to the Equation (4). In the MPD-TFRs presented, the fatigued and the unfatigued signals can be differentiated, especially by the spectrum occurring between 200 and 300 μs.

A comparison of the MPD performance in the presence and absence of noise can be compared using the MPD-TFR plots presented in Figures 3 and 4. Even with 0 dB SNR, the MPD reconstruction of the signal was fairly good and the MPD-TFR shows distinction between the fatigued and the unfatigued models.

The number of MPD iterations (N) was chosen to be 10. Figures 5(a) and 5(b) show the residue energy after every MPD iteration for the first 30 iterations. For a 20 dB signal, the residue at the end of 30 iterations is about 1% of the total signal energy and is much less than 10% after 10 iterations. However, this perfect fitting may be an over-fitting of the data and there may be components of noise present in the reconstructed signal. It was experimentally observed that the information after 10 iterations was sufficient with highly reduced noise. This observation may be further extended to the 0 dB signals. In this case, the residue is considerably higher and after 10 iterations, it is about 50% of the total signal energy. In addition, we may observe that the decay rate of the residue is slower in the noisy signal when compared to the noiseless one. Figures 5(c)- 5(f) show the MPD-TFR when $N = 30$ iterations were used to reconstruct the signal. When compared to Figures 3 and 4, we noticed an increased ambiguity between the damage classes.

3.3 Choice of Parameters for HMM Classifier

In this application, we built two HMMs, one for the fatigued class and one for the unfatigued one. Out of the 450 waveforms generated, 150 was used for training the HMMs as described in Section 2.2. However, there were certain assumptions that were involved in the parameter estimation of the HMMs. It was decided with the aid of a few MPD-TFR plots that a 3 state HMM would work acceptably. The observation sequences were sorted according to the time shifts τ. The states were depicted as instants of time where the signal time-frequency behavior did not change considerably. An example is demonstrated in Figure 6. Here, the vertical dotted lines (at 180 and 280 μs) represent the state separation. The observation before 180 μs is associated to state 1 of the signal, 180-280 μs is state 2 and beyond 280 μs is state 3 of the sequence.

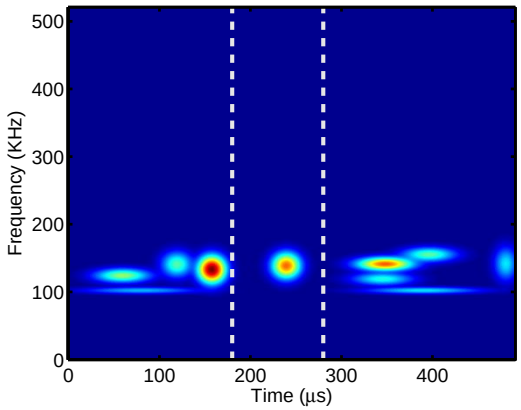

Figure 6. Choice of HMM states.

The observation vectors were quantized to finite codes. We chose 16 codes (4 bit information). Thirty EM iterations were chosen for the value of $\boldsymbol{\theta}_{ML}$ to converge from an initial guess to the final maximum likely estimate. The parameter estimates were chosen by multiple trials by testing the models on a validation data of size 300 (150 from each class) observation sequences that were not used in the training. Model validation involved classifying (as described in Section 2.3) the set of sequences and evaluating the performance of the classifiers. The parameters were tuned for optimize the classifier in terms of correct classification rate and speed.

Finally, the performance of the classifier was tested on the remaining 150 waveforms from each class. The results of the classification was tabulated. Training and validation was done using 20 dB signals. Testing involved signals of all other SNRs.

3.4 Classification Result

We used signals from all the available SNRs of -3 through 5 dB, 10 dB, 15 dB and 20 dB. We have presented the classification result in a confusion matrix. In a confusion matrix $\mathcal{C}$, $c(i,j)$ represent the probability that a signal belonging to class i gets classified as class j. The entries along the diagonal of $\mathcal{C}$ represent the probability of correct classification for a given class, and a sum of the off-diagonal entries along a row gives the probability of miss-classification for a given class of signals. For example, Table 1(a) shows the confusion matrix for the dataset with SNR = 0 dB. According to this table, the unfatigued dataset has a correct classification rate of 93.3% and fatigued dataset has a correct classification rate of 73.33%. Thus, the average correct classification for signals with SNR = 0 dB is 83.33%.

(a) SNR = 0 dB

	U	F
U	0.9333	0.0667
F	0.2667	0.7333

(b) SNR = 5 dB

	U	F
U	1.0000	0.0000
F	0.1000	0.9000

(c) SNR = 10 dB

	U	F
U	1.0000	0.0000
F	0.0533	0.9467

(d) SNR = 20 dB

	U	F
U	1.0000	0.0000
F	0.0000	1.0000

Table 1. Confusion matrices for different SNRs (U: unfatigued, F: fatigued).

Table 1 summarizes the classification results. With an improvement in the SNR, the correct classification rate of the described HMM based classifier improves. This is an expected result. The correct classification rates at 5 dB, 10 dB and 20 dB SNRs are 95%, 97.34% and 100% respectively. It may be observed that the performance of the classifier favored the unfatigued class.

This performance was based on a specific classification threshold. By varying this threshold, the probability of correct classification can be altered. A plot of probability correct classification against probability of false alarm (miss-classification) given a particular class for all possible thresholds is called a receiver operating characteristic (ROC) curve. The confusion matrix presented the performance at a specific point on this curve. The ROC curves of this classifier under the given assumption of unfatigued class is presented in Figure 7. By correct classification here we mean that signals actually from the damaged class are correctly classified as being from the damaged class. By false alarm here, we imply that a damage was detected when there was actually no damage. In classification performance improves with increasing SNR.

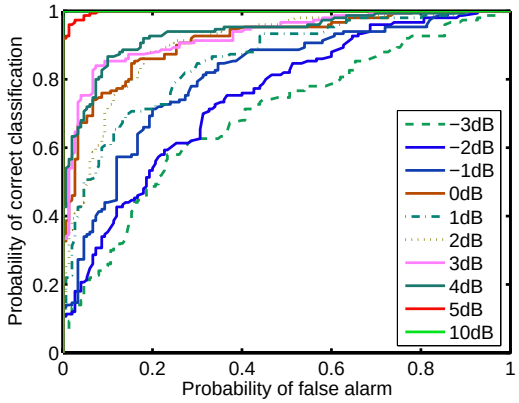

Figure 7. Receiver operative characteristic (ROC) curves for different SNRs.

4. CONCLUSION

In this work, we presented physics based modeling of a lug joint sample. The matching pursuit decomposition was used to extract time-frequency damage features from the modeled signals in order to train the HMM based classification algorithm. Different realizations of the signals at various noise levels were used to test the proposed HMM based classification technique. The discrete HMM based damage classifier is observed to be quite robust to noise. Performance was very good (high correct classification rates), even for the low operating SNR values. When applied to the classification of crack damage in lug joint, the performance was good (over 90% correct classification) even for high levels of noise.

Currently we are working on training the HMM classifier on physics based FEM modeled data and then test the classifier using data collected from real experiments.

ACKNOWLEDGMENTS

This research was supported by the MURI Program, Air Force Office of Scientific Research, grant number: FA9550-06-1-0309; Technical Monitor, Dr. Victor Giurgiutiu.

REFERENCES

[1] Farrar, C. R. and Worden, K., "An introduction to structural health monitoring," *Philosophical Transactions of the Royal Society A* **365**, 303–315 (2007).

[2] Farrar, C. R. and Lieven, N. A. J., "Damage prognosis: the future of structural health monitoring," *Philosophical Transactions of the Royal Society A* **365**, 623–632 (2007).

[3] Staszewski, W. J., Boller, C., and Tomlinson, G. R., [*Health Monitoring of Aerospace Structures*], Wiley, England (2003).

[4] Zhou, W., Chakraborty, D., Kovvali, N., Papandreou-Suppappola, A., Cochran, D., and Chattopadhyay, A., "Damage classification for structural health monitoring using time-frequency feature extraction and continuous hidden markov models," *Asilomar Conference on Signals, Systems, and Computers*, 848–852 (November 2007).

[5] Kovvali, N., Das, S., Chakraborty, D., Cochran, D., Papandreou-Suppapola, A., and Chattopadhyay, A., "Time-frequency based classification of structural damage," *48th AIAA/ASME/ASCE/AHS/ASC Structures, Structural Dynamics, and Materials Conference* (2007).

[6] Zhou, W., Kovvali, N., Papandreou-Suppappola, A., Cochran, D., and Chattopadhyay, A., "Hidden Markov model based classification of structural damage," *Proc. of SPIE* **6523**, 652311 (2007).

[7] Mallat, S. G. and Zhang, Z., "Matching pursuits with time-frequency dictionaries," *IEEE Transactions on Signal Processing* **41**, 3397–3415 (1993).

[8] Giurgiutiu, V., "Lamb wave generation with piezoelectric wafer active sensor for structural health monitoring," *Smart Structures and Materials: Smart Structures and Integrated Systems* **111** (2003).

[9] Giurgiutiu, V., Bao, J., and Zhao, W., "Piezoelectric wafer active sensor embedded ultrasonics in beams and plates," *Experimental Mechanics* **43**(4), 428–449 (2003).

[10] Giurgiutiu, V., Zagrai, A. N., Bao, J., Redmond, J., Roach, D., and Rackow, K., "Active sensors for health monitoring of aging aerospace structures," *International Journal of the Condition Monitoring and Diagnostic Engineering Management* **5**(3) (2002).

[11] Ihn, J. B. and F.K., C., "Pitch-catch active sensing methods in structural health monitoring for aircraft structures," *Structural Health Monitoring* **7**(1), 5–19 (2008).

[12] Soni, S., Wei, J., Chattopadhyay, A., and Peralta, P., "Multi-scale modeling and experimental validation for component fatigue life prediction," *Proceedings of ASME IMECE* (2007).

[13] Simulia World Headquarters, P., "Abaqus version 6.7, abaqus/cae and abaqus/standard," (2007).

[14] Rabiner, L. R. and Juang, B. H., "An introduction to hidden Markov models," *IEEE ASSP Magazine* , 4–15 (1986).

[15] Rabiner, L. R., "A tutorial on hidden Markov models and selected applications in speech recognition," *Proceedings of the IEEE* **77**, 257–286 (1989).

[16] Hlawatsch, F. and Boudreaux-Bartels, G., "Linear and quadratic time-frequency signal representations," *IEEE Signal Processing Magazine* **9**, 21–67 (April 1992).
[17] Dempster, A., Laird, N., and Rubin, D., "Maximum likelihood from incomplete data via the EM algorithm," *Journal of the Royal Statistical Society, Series B* **39**, 1–38 (1977).
[18] Rose, J. L., ed., [*Ultrasonic Waves in Solid Media*], University Press, Cambridge, Cambridge (1999).
[19] Papandreou-Suppappola, A., ed., [*Applications in Time-Frequency Signal Processing*], CRC Press, Florida (2002).
[20] Papandreou-Suppappola, A. and Suppappola, S. B., "Adaptive time-frequency representations for multiple structures," in [*Proc. 10th IEEE Workshop on Statistical Signal and Array Processing*], **3** (2000).